

## Phase diagrams of shape-anisotropic colloidal particles

M. DIJKSTRA

*Soft condensed matter group, Debye Institute for NanoMaterials Science, Utrecht University  
Princetonplein 5, 3584 CC Utrecht, The Netherlands*

**Summary.** — In order to predict the equilibrium phase behaviour of colloidal particles, one should first identify the “candidate” structures in which the particles may assemble. Subsequently, the free energy of the candidate structures should be determined to establish the thermodynamically stable phases and to map out the bulk phase diagram. Here, we describe a simple method based on a simulated annealing approach to predict candidate structures and several techniques to calculate the free energy of a thermodynamic system and to map out the phase diagram. Exemplarily, we present phase diagrams of several shape-anisotropic hard particles, *e.g.*, hard dumbbells, hard bowl-shaped particles, and hard oblate spherocylinders.

### 1. – Introduction

Colloidal suspensions consist of mesoscopic particles with sizes in the range of a few nanometers to a few micrometers, which are dispersed in a fluid medium. Colloidal particles are larger than solvent molecules, but small enough to undergo Brownian motion. This highly irregular movement of the suspended particles, named after the Scottish botanist Robert Brown, is caused by the constant bombardment of the solvent molecules onto the colloidal particle surfaces. Brownian motion allows particles to explore phase space and to self-assemble into equilibrium structures, such as three-dimensional ordered

crystal phases, liquid crystalline phases, and disordered liquids. However, they can also form non-equilibrium structures like glasses or gel-like structures. Colloidal systems behave similarly to ordinary atomic and molecular systems, and can serve as important model systems for condensed matter physics. Studies of colloidal suspensions have indeed provided us with a wealth of insight into physical phenomena such as melting, (de)mixing, freezing, nucleation, glass transitions, gelation, and structure formation, either spontaneous or externally driven by templates, gravity, or electric fields. Moreover, the much larger size of colloids compared to atoms allows for an unprecedented degree of manipulation, visualization, and control.

More importantly, recent advances in the chemical synthesis and fabrication of colloidal particles have resulted in a spectacular variety of new colloidal building blocks [1,2] including a huge number of shape-anisotropic particles such as rods [3-5], plates [6], colloidal molecules [7,8], bead chains, dumbbells [9], hollow objects, microcapsules, patchy particles, cubes [10-14], superballs [15,16], octahedra [13,14,17,18], tetrahedra [19,20], octapods [21-23], tetrapods [24,25], nanostars [26-28], and colloidal caps [29-31].

The main challenge now is to exploit this huge variety of available colloidal building blocks and to self-assemble them into structured arrangements for advanced and functional materials and devices. The fabrication of these so-called “nanomaterials” with a well-defined structure on the scale of tens to hundreds of nanometers, makes these materials perfectly suited for the manipulation of (visible) light. Hence, colloidal crystals with lattice spacings similar to the wavelength of light are considered to be prime candidates for the fabrication of photonic band-gap materials [32-35] with potential applications in highly efficient light-emitting diodes (LEDs), solar cells, sensors, and optical computer chips. Additionally, nanomaterials with the right properties are likely to be instrumental in the development of new photovoltaic cells [36,37] and electronic displays [38,39]. The potential use of the spontaneous self-organisation of colloids as a promising and inherent cheap route for the fabrication of nanostructures requires not only the ability to tune the properties of the colloidal building blocks, but also a better understanding of the relation between the building blocks, their interactions, and the self-assembled structures.

Additionally, the tunability of the effective interactions between the colloidal particles offer great opportunities. To be more specific, colloidal particles with anisotropic interactions can be synthesized by controlling the shape of the particles, or by creating “patches” on the surface of the particles. The interactions between the particles can also be altered by modifying the dispersive medium, *i.e.*, addition of salt to the dispersion leads to screening of the electrostatic interactions, the presence of non-adsorbing polymer results in effective depletion attractions, and critical Casimir forces arises due to the confinement of long-range density fluctuations when the host fluid is close to a critical point. One can further modify the interaction by application of, *e.g.*, external electric and magnetic fields, templates, gravity, etc.

Exploiting the self-assembly of these novel colloidal building blocks calls for theoretical tools to predict the structure and phase behavior of these particles. Predicting the equilibrium phase behaviour of colloidal particles can be divided into three parts: i) First, one should identify the possible “candidate” structures in which the particles with given

interactions and system parameters may assemble, ii) subsequently, the free energy of the identified candidate structures should be determined to establish the thermodynamically stable phases and to map out the full equilibrium phase diagram, and iii) finally, one should investigate the kinetic pathways to form the thermodynamically stable phases, as the self-assembly may be suppressed by kinetic effects such as vitrification, gelation, defects and stacking faults. Below, we briefly describe an efficient simulation method to predict candidate structures and several techniques to calculate the free energy of a system. A natural starting point to study the self-assembled structures of these shape-anisotropic colloidal building blocks is to view them as hard particles [1]. Not only can these hard-particle models be used to predict properties of suitable experimental systems, but such models also provide a stepping stone towards systems where soft interactions play a role [40,41]. Additionally, the analysis of hard particles is of fundamental relevance and raises problems that influence fields as diverse as (soft) condensed matter [1,35,42,43], mathematics, [42, 44] and computer science [45]. The concurrent boom in simulation studies of hard anisotropic particles is thus not surprising [42-44, 46-54]. In the last section, we present several phase diagrams of shape-anisotropic hard particles that have been determined using free-energy calculations in Monte Carlo simulations.

## 2. – Predicting candidate crystal structures

Predicting the structures that will be formed is vital for exploiting self-assembly and a major computational challenge. In a recent Review article, Woodley and Catlow [55] claimed “The prediction of structure at the atomic level is one of the most fundamental challenges in condensed matter science”, and Maddox stated in a News and Views Nature article [56] “One of the continuing scandals in the physical sciences is that it remains in general impossible to predict the structure of even the simplest crystalline solids from a knowledge of their chemical composition”. Hence, it is not surprising that the subject of crystal structure prediction has received much attention from the scientific community over the last several decades. The question itself is deceptively simple: assuming that the underlying interactions between constituent particles are known, which crystal structures are stable? Conventional methods are often based on a pre-selection of candidate structures for which the (free) energies are calculated to determine the thermodynamically most stable phase. The pre-selection of structures relies heavily on intuition, trial and error, and experience. A serious drawback of the pre-selection is that it immediately rules out all non-selected structures at the very beginning, which might include the stable equilibrium structures. Hence, it is expected that this pre-selection strategy fails dramatically for the new anisotropic colloidal building blocks for which novel and more exotic structures are envisaged.

In 1990, Pannetier *et al.* proposed a method based on simulated annealing techniques [57]. In their method a general crystal structure was described in terms of lattice and basis vectors, and the “cost” function for the system was minimized using simulated annealing. The method can easily be extended to any atomic system for which a suitable cost function, *e.g.*, the potential energy, can be constructed [58]. Recently, more

advanced minimization techniques such as genetic algorithms [59-61] and Monte Carlo (MC) basin hopping algorithms [62] have been applied. Typically these techniques are used to locate the minimum potential energy of the system, and as such, probe the zero-temperature phase behavior. However, for systems where the entropy plays a significant role, these techniques break down. For instance, new crystal structures can appear in the phase diagram at finite temperature, which are different from the zero-temperature crystal structures, and hence predicting the zero-temperature structures will not be sufficient for making predictions at finite temperature. Additionally, for hard systems the potential energy is always zero as only non-overlapping configurations contribute to the partition function, and crystal structures are thus stabilized by entropy alone. For such systems it is difficult to construct an appropriate cost function, and therefore the MC basin hopping algorithm and genetic algorithms cannot be applied to hard-core systems.

Recently, Filion *et al.* proposed an efficient simulation method, which is based on a simulated annealing approach, to predict crystal structures at finite temperatures and finite pressures for a wide variety of systems, including hard-core systems whose phase behavior is purely entropy-driven [63]. This method was applied to spheres with different types of interactions such as hard, attractive, anisotropic interactions, semi-long-range soft interactions, truly long-range interactions using Ewald sums [63], and patchy interactions [64]. Additionally, the algorithm was applied to predict the best packing of a huge variety of shape-anisotropic particles [65]. This technique is similar in approach to the metadynamics method [66], but uses compression from the fluid phase and Monte Carlo (MC) sampling in a variable simulation box to determine candidate structures. This technique, also referred to as the “floppy-box” Monte Carlo (FBMC) method, has proven to be remarkably efficient and robust, and has led to the discovery of an astonishing variety of new crystal structures for a wide range of systems, thereby demonstrating its effectiveness for the novel colloidal building blocks that have become available experimentally [63-65].

The FBMC algorithm is an ordinary isothermal-isobaric ( $NPT$ ) ensemble Monte Carlo (MC) simulation with three important features that makes it an efficient tool to predict candidate structures. First, the number of particles  $N$  is small, typically  $1 \leq N \leq 12$ . Second, the three lattice vectors  $\vec{L}$  comprise the simulation box and are allowed to vary independently of each other in both their length and orientation. As in a standard  $NPT$ -MC simulation, each MC cycle consists of a trial move to displace a particle and a trial move to change the volume of the simulation box where the acceptance rules of the particle and volume moves are given by the Metropolis algorithm [67]. In order to allow for box shape fluctuations, a trial volume move involves an attempt to change the orientation and the length of a random lattice vector. This is the origin of the term “floppy box”, which was adopted to emphasize that the box does not have a fixed shape. We also remark that the FBMC method is similar to other variable-box-shape methods [66, 67, 44], and note that an  $NPT$  variable-box shape simulation is essentially an isothermal-isotension simulation with a fixed isotropic stress tensor, that is directly proportional to the pressure [67]. Third, to predict candidate structures the simulation is preceded by a compression from a disordered fluid phase. To this end, the initial

pressure is chosen to be below the fluid to solid transition and the pressure is increased incrementally until the system solidifies. An essential feature of the FBMC method is that due to the small number of particles and the variable box shape, the simulation box essentially acts as a “unit cell” for the crystal structures. However, working with small simulation boxes, and allowing the shape of the simulation box to fluctuate introduces new problems. The main problem is that while the system is in the fluid phase, the shape of the box fluctuates significantly. Thus, the box can become extremely distorted, which makes the potential energy summation time consuming. To avoid this problem, one may use the lattice reduction technique described in ref. [61] to redraw the unit cell when it becomes too distorted. Additionally, one can impose a restriction on all angles and lengths of the lattice vectors to avoid trivial unphysical crystal structures. For instance, one may exclude angles less than  $30^\circ$  and greater than  $150^\circ$ . Without these restrictions the particles tend to line up in columns, such that the particles only interact with their own periodic images in one of the lattice directions resulting in unphysical contributions to the entropy. Such a condition prevents the box (particularly while in the fluid phase) from an extreme distortion, while allowing for all possible crystal phases to emerge in the FBMC simulations. Finally, to effectively predict candidate crystal structures it is necessary to perform FBMC simulations for the same system many times with different random seeds, starting configurations, initial conditions, compression paths, etc. This usually results in a set of candidate crystal structures for which the frequency of occurrence in the FBMC runs gives some insight in the stability of the structures [63]. In order to determine quickly whether or not a candidate structure is mechanically stable, one may perform a simulation of such a structure with a much larger system size ( $\sim 1000$ – $10000$  particles) than employed in the FBMC method. If the candidate structure deforms into another crystal structure or melts into a fluid phase, the candidate structure is thermodynamically unstable. However, we stress that only free-energy calculations can demonstrate conclusively the thermodynamic stability of candidate structures.

### 3. – Free-energy calculations and phase diagrams

The aforementioned FBMC method and alternative algorithms can be employed to predict candidate crystal phases for a given system. Subsequently, the predicted structures can be used in free-energy calculations to determine the thermodynamically most stable phases and to map out the bulk phase diagram. Below, we describe in more detail how the free energy can be calculated in Monte Carlo simulations using the thermodynamic integration technique. In this method, one constructs a reversible path that links the system of interest to a reference system for which the free energy is known. However, the free energy is known explicitly for only a few systems. To compute the Helmholtz free energy of a dense fluid, one may construct a reversible path from the system of interest to the ideal gas phase. However, for a solid, a direct path to the ideal gas without crossing a phase transition is usually not possible, and one often employs the Einstein crystal as a reference state.

**3.1. Fluid phase.** – The Helmholtz free energy for the fluid phase can be determined by integrating the equation of state (EOS), *i.e.*, the pressure as a function of density  $P(\rho)$  with  $\rho = N/V$  the number density,  $N$  the number of particles, and  $V$  the volume. To this end, one constructs a reversible path to an infinitely dilute gas phase. The EOS of the fluid phase can be obtained by employing standard  $NPT$  Monte Carlo simulations and measuring the averaged density  $\rho$  for a range of pressures  $P$ . The Helmholtz free energy  $F$  of the fluid phase is then determined by

$$(1) \quad \frac{\beta F(\rho)}{N} = \frac{\beta F^{id}(\rho)}{N} + \int_0^\rho \left( \frac{\beta P(\rho') - \rho'}{\rho'^2} \right) d\rho',$$

where  $\beta = 1/k_B T$ ,  $k_B$  equals Boltzmann's constant,  $T$  the temperature,  $\beta F^{id}(\rho) = N \log[\rho \Lambda^3] - N$  is the free energy of an ideal gas at density  $\rho$ ,  $\Lambda = (h^2/2\pi m k_B T)^{1/2}$  denotes the de Broglie wavelength,  $m$  the mass of the particle, and  $h$  Planck's constant. Alternatively, one can also construct a reversible path to a fluid phase at density  $\rho_0$  for which one can compute the chemical potential  $\mu(\rho_0)$  using Widom's particle insertion method [67]. Using  $\mu(\rho_0)$  and  $P(\rho_0)$ , it is straightforward to determine the Helmholtz free energy  $F(\rho_0)/N = \mu(\rho_0) - P(\rho_0)/\rho_0$  at density  $\rho_0$  [67]. The Helmholtz free energy  $F(\rho)$  at density  $\rho$  can then be obtained by integrating the equation of state:

$$(2) \quad \frac{\beta F(\rho)}{N} = \frac{\beta F(\rho_0)}{N} + \int_{\rho_0}^\rho \left( \frac{\beta P(\rho')}{\rho'^2} \right) d\rho'.$$

We note that this thermodynamic integration route is not restricted to the fluid phase, but can also be employed for a solid, liquid crystalline, or any other phase.

**3.2. Crystal phase.** – The Helmholtz free energy  $F$  of a crystal phase can be calculated using the Frenkel-Ladd method [68]. Here, one constructs a reversible path from the crystal of interest to a non-interacting Einstein crystal for which one can calculate the free energy exactly. In the Einstein crystal, the center-of-mass of the particles are fixed to their ideal lattice positions using harmonic springs in such a way that the particles do not interact with each other. The lattice positions of the Einstein crystal should resemble the equilibrium positions of the particles in the crystal phase of interest. The equilibrium position for each particle can be obtained by averaging the instantaneous positions of the particles in a simulation of the crystal structure. Using the Einstein crystal as a reference state, the next step is to construct a reversible path from the crystal phase to the Einstein crystal without crossing a first-order phase transition. For a system of particles that interacts via hard-core potentials, one can switch on the harmonic springs, while keeping the hard-core interactions between the particles. To this end, one introduces the auxiliary Hamiltonian

$$(3) \quad \beta H(\mathbf{r}^N; \lambda) = \sum_{i < j} \beta \phi_{hc}(\mathbf{r}_i, \mathbf{r}_j) + \lambda \sum_{i=1}^N \frac{(\mathbf{r}_i - \mathbf{r}_{i,0})^2}{\sigma^2},$$

where  $\mathbf{r}_i$  is the center-of-mass position of particle  $i$ ,  $\mathbf{r}_{i,0}$  is the ideal lattice position of

particle  $i$ ,  $\lambda$  is the dimensionless spring constant or coupling parameter,  $\sigma$  the size of the particle, which is taken to be the unit of length, and  $\phi_{hc}(\mathbf{r}_i, \mathbf{r}_j)$  is the hard-core interaction between particle  $i$  and  $j$ . The usual thermodynamic integration path for hard particles consists of a gradual increase of  $\lambda$  from 0 (the system of interest) to  $\lambda_{\max}$ . For sufficiently high  $\lambda_{\max}$ , the particles are bound so strongly to their lattice sites that they do not feel each other, and the system reduces to a non-interacting Einstein crystal. Consequently, the free energy of the crystal phase  $F(N, V, T)$  is then given by

$$(4) \quad \beta F(N, V, T) = \beta F_{\text{Einst}}(N, V, T) - \int_0^{\lambda_{\max}} d\lambda \left\langle \frac{\partial \beta F}{\partial \lambda} \right\rangle,$$

where the free energy of the ideal Einstein crystal  $F_{\text{Einst}}(N, V, T)$  with the center-of-mass correction terms reads [67]:

$$(5) \quad \beta F_{\text{Einst}}(N, V, T) = -\frac{3(N-1)}{2} \ln \left( \frac{\pi}{\beta \lambda_{\max}} \right) + N \ln \left( \frac{\Lambda^3}{\sigma^3} \right) + \ln \left( \frac{\sigma^3}{V N^{1/2}} \right).$$

The integrand  $\langle \partial \beta F / \partial \lambda \rangle = \langle \sum_{i=1}^N (\mathbf{r}_i - \mathbf{r}_{0,i})^2 / \sigma^2 \rangle$  in eq. (4) can be calculated in an MC simulation of a system that is described by the Hamiltonian (3) for fixed values of  $\lambda$  in the range  $\lambda \in [0, \lambda_{\max}]$  with the constraint that the center-of-mass of the solid is fixed in order to avoid an unwanted drift of the solid in the limit  $\lambda \rightarrow 0$ .

If we consider anisotropic particles rather than spherical particles, the crystal phase possess internal degrees of freedom in addition to translational degrees of freedom. In this case, each particle  $i$  possess  $d$  configurational degrees of freedom, which we denote by a  $d$ -dimensional vector  $\mathbf{q}_i$ . For spherical particles in three spatial dimensions, each particle  $i$  is described by the center-of-mass position, yielding  $\mathbf{q}_i \equiv \mathbf{r}_i$ , and the number of degrees of freedom equals  $d = 3$ . Uniaxial anisotropic particles can be characterized by a unit vector  $\hat{u}$  to denote the orientation of the symmetry axis, and possess two orientational degrees of freedom in addition to the translational degrees of freedom, which yields  $d = 5$ . Anisotropic particles without any axes of symmetry have three rotational degrees of freedom and should be described by two perpendicular unit vectors or in terms of the three Eulerian angles  $(\theta, \phi, \chi)$ , resulting in  $d = 6$ . As a consequence, the crystal phase of anisotropic particles exhibits internal degrees of freedom in addition to the translational degrees of freedom, which may give rise to a wide variety of new crystal phases. However, for crystal structures consisting of anisotropic particles, the thermodynamic integration route as discussed above may fail as the system will never reach the limit of a non-interacting Einstein crystal due to the orientational degrees of freedoms of the hard-core particles. Below, we describe two methods to construct a reversible path from a crystal phase consisting of *anisotropic* particles to a non-interacting Einstein crystal.

**3.3. Plastic crystal phases.** – For crystal structures consisting of freely rotating anisotropic particles, so-called plastic crystal or rotator phases, the thermodynamic integration method (4) may fail if the system remains interacting due to particle rotations for infinite

values of the spring constant  $\lambda$ . The Einstein integration method can then be combined with an additional thermodynamic integration path, which changes gradually the hard-core system into a non-interacting system. To this end, one approximates the hard-particle potential  $\phi_{hc}(\mathbf{q}_i, \mathbf{q}_j)$  by an penetrable interaction potential  $\varphi(i, j)$ , where we use the shorthand notation  $\varphi(i, j) = \varphi(\mathbf{q}_i, \mathbf{q}_j)$ . the translational and orientational degrees of freedom of particle  $i$  are denoted by  $\mathbf{q}_i$ . The Hamiltonian is now given by

$$(6) \quad \beta H(\mathbf{q}^N; \lambda, \gamma) = \gamma \sum_{i < j}^N \beta \varphi(i, j) + \lambda \sum_{i=1}^N \frac{(\mathbf{r}_i - \mathbf{r}_{i,0})^2}{\sigma^2},$$

where

$$(7) \quad \beta \varphi(i, j) = \begin{cases} 1 - A\zeta(i, j) & 0 \leq \zeta(i, j) < 1, \\ 0, & \text{otherwise,} \end{cases}$$

with  $\gamma$  the integration parameter and  $A$  an adjustable parameter, which is kept fixed during the simulation at a value of, say  $A = 0.9$  [69]. In the limit  $\gamma \rightarrow \infty$  the pair potential reduces to the hard-core interaction, but convergence of the thermodynamic integration is often already obtained for lower values of  $\gamma_{\max}$ . This method allows us thus to change gradually from a non-interacting system,  $\gamma = 0$ , to a crystal phase of (freely rotating) hard particles when  $\gamma_{\max}$  is sufficiently high. In order to minimize the error and maximize the efficiency of the free-energy calculation, the penetrable potential  $\varphi(i, j)$  must decrease if the volume with which the particles overlap decreases and the potential must exhibit a discontinuity when the particles are just at contact [69]. In this case, the amount of overlap and the number of overlaps decrease smoothly upon increasing  $\gamma$ . To achieve this, one defines  $\zeta(i, j)$  in such a way that it is zero, when particles  $i$  and  $j$  are fully overlapping, and one when particles  $i$  and  $j$  are just at contact. This thermodynamic integration path was introduced in ref. [69] for hard spheres, and subsequently extended to hard dumbbells and hard superballs in refs. [53, 70]. For hard spheres with diameter  $\sigma$ , one may use  $\zeta(i, j) = (r_{ij}/\sigma)^2$ , which is zero when the two spheres are at center-of-mass distance  $r_{ij} = |\mathbf{r}_i - \mathbf{r}_j| = 0$  and thus right on top of each other, and one when the particles are just at contact, *i.e.*  $r_{ij} = \sigma$ . A similar approach was employed for hard dumbbells, where the individual spheres of each dumbbell interact with this penetrable pair potential. In the case of superballs, one may take  $\zeta(i, j)$  to be equal to the scaling factor with which the size of particle  $i$  and  $j$  should be scaled uniformly to bring the particles just in contact provided the original positions and orientations are kept fixed. With this choice, one finds again that for fully overlapping particles,  $\zeta(i, j) = 0$  as the particle sizes should be scaled by 0 to remove the overlap, and  $\zeta(i, j) = 1$  when the particles are just at contact.

In order to obtain the Helmholtz free energy of the crystal phase, one has to integrate over both paths to determine the free energy difference between the system of interest and the non-interacting Einstein crystal. Starting at a very high value of  $\gamma_{\max}$  where the particles behave as hard particles, one can turn on the springs that couple the particles

to their respective lattice positions by increasing  $\lambda$  from 0 to  $\lambda_{\max}$ . Subsequently, one can then decrease  $\gamma$  from  $\gamma_{\max}$  to 0 such that the system reduces to an ideal Einstein crystal. The Helmholtz free energy  $F$  of the crystal is then obtained by integrating over both paths

$$(8) \quad \beta F(N, V, T) = \beta F_{\text{Einst}}(N, V, T) - \int_0^{\lambda_{\max}} d\lambda \left\langle \frac{\partial \beta F}{\partial \lambda} \right\rangle_{\gamma_{\max}} + \int_0^{\gamma_{\max}} d\gamma \left\langle \frac{\partial \beta F}{\partial \gamma} \right\rangle_{\lambda_{\max}},$$

where  $\langle \partial \beta F / \partial \lambda \rangle = \langle \sum_{i=1}^N (\mathbf{r}_i - \mathbf{r}_{0,i})^2 / \sigma^2 \rangle$  and  $\langle \partial \beta F / \partial \gamma \rangle = \langle \sum_{i < j}^N \beta \varphi(i, j) \rangle$ . We note that for particles with  $d_r$  rotational degrees of freedom, the Helmholtz free energy of an non-interacting Einstein crystal (5) includes an extra term  $\sum_{k=1}^{d_r} N \ln \mathcal{V}_k$  due to the integration over the angular momenta [71]. Here  $\mathcal{V}_k = (h^2 / 2\pi I_k k_B T)^{1/2}$  and  $I_k$  is the corresponding moment of inertia.

**3.4. Orientationally ordered crystal phases.** – For crystal structures consisting of anisotropic particles that display orientational order, one may add an aligning potential that fixes the orientations of the particles to the orientations of the ideal crystal lattice in order to reach the non-interacting Einstein crystal [72]. Using the same coupling constant  $\lambda$  that attaches the particles to their lattice sites, the Hamiltonian is now given by

$$(9) \quad \beta H(\mathbf{q}^N; \lambda) = \lambda \sum_{i=1}^N \left[ \frac{(\mathbf{r}_i - \mathbf{r}_{i,0})^2}{\sigma^2} + \sin^2 \psi_{i,a} + \sin^2 \psi_{i,b} \right],$$

where the angles  $\psi_{i,a}$  and  $\psi_{i,b}$  are the minimum angles between the orientation of particle  $i$  and the respective orientations, say  $\mathbf{a}$  and  $\mathbf{b}$ , of particle  $i$  in the ideal crystal lattice. The coupling parameter  $\lambda$  controls the strength of both external potentials; hence for  $\lambda = 0$  the system reduces to the crystal structure of interest, and for  $\lambda = \lambda_{\max}$  with  $\lambda_{\max}$  sufficiently large, the system reduces to a non-interacting Einstein crystal. The Helmholtz free energy of the crystal phase can then be obtained using eq. (4) with  $\langle \partial \beta F / \partial \lambda \rangle = \langle \sum_{i=1}^N (\mathbf{r}_i - \mathbf{r}_{0,i})^2 / \sigma^2 + \sin^2 \psi_{i,a} + \sin^2 \psi_{i,b} \rangle$ . The Helmholtz free energy of the non-interacting Einstein crystal  $F_{\text{Einst}}$  reads

$$(10) \quad \beta F_{\text{Einst}}(N, V, T) = -\frac{3(N-1)}{2} \ln \left( \frac{\pi}{\beta \lambda_{\max}} \right) + N \ln \left( \frac{\Lambda^3}{\sigma^3} \right) \\ + \sum_{k=1}^{d_r} N \ln \mathcal{V}_k + \ln \left( \frac{\sigma^3}{V N^{1/2}} \right) \\ - \sum_{i=1}^N \ln \left\{ \frac{1}{8\pi^2} \int \exp [-\lambda_{\max} (\sin^2 \psi_{i,a} + \sin^2 \psi_{i,b})] \sin \theta d\theta d\phi d\chi \right\},$$

where the latter term is the free energy due to the aligning field, which can be estimated numerically by integrating the respective partition function over all the particle orientations described by the Eulerian angles  $\theta$ ,  $\phi$ , and  $\chi$ .

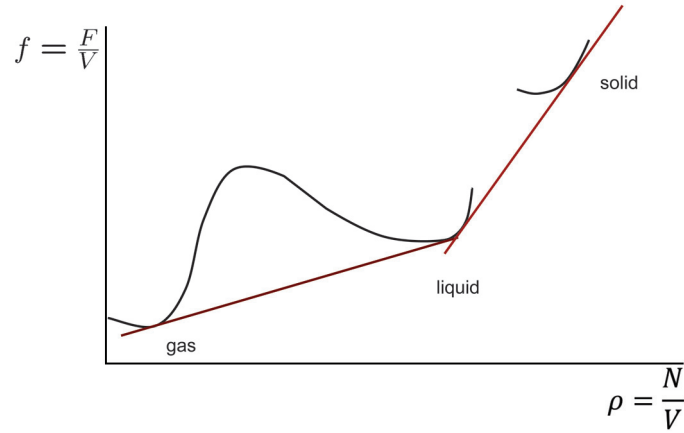


Fig. 1. – The free-energy density  $f = F/V$  versus the density  $\rho$ , showing the existence of a symmetry-conserving gas-liquid transition at low densities and a symmetry-breaking liquid-solid transition at higher densities. Schematic illustration of the common tangent construction to determine phase coexistence.

**3.5. Mapping out phase diagrams.** – In order to establish the thermodynamic stable phases and to determine the equilibrium phase diagram, one should first determine the Helmholtz free energy  $F(N, V, T)$  of the identified candidate phases using the thermodynamic integration techniques as discussed above. Since  $F$  is an extensive quantity for macroscopically large  $N$  and  $V$ , it is convenient to define a free-energy density  $f(\rho, T) = F/V$ . Both the pressure and the chemical potential are important quantities in the determination of phase boundaries at first-order transitions. The pressure  $P$  is given by  $P(\rho, T) = -(\partial F/\partial V)_{N, T} = -f + \rho(\partial f/\partial \rho)_T$  and the chemical potential  $\mu$  reads  $\mu(\rho, T) = (\partial F/\partial N)_{V, T} = (\partial f/\partial \rho)_T$ . The conditions for coexistence of phase I and phase II with densities  $\rho_I$  and  $\rho_{II}$  are thermal equilibrium  $T_I = T_{II}$ , mechanical equilibrium  $P_I(\rho_I) = P_{II}(\rho_{II})$  and chemical equilibrium  $\mu_I(\rho_I) = \mu_{II}(\rho_{II})$ . Invoking these two conditions at fixed temperature yields

$$(11) \quad \left. \frac{\partial f}{\partial \rho} \right|_{\rho_I} = \left. \frac{\partial f}{\partial \rho} \right|_{\rho_{II}} = \frac{f(\rho_{II}) - f(\rho_I)}{\rho_{II} - \rho_I}.$$

Geometrically this representation corresponds to the so-called common tangent construction for determining  $\rho_I$  and  $\rho_{II}$ . This is illustrated in fig. 1, where we plot schematically  $f(\rho)$  for a symmetry-conserving gas-liquid transition at low densities and a symmetry-breaking liquid-solid transition at higher densities. The physical interpretation of the common tangent construction, denoted by the red solid lines in fig. 1, shows that the system can lower its free energy by forming a linear combination of two coexisting phases. Finally it is straightforward to show that adding terms to  $F$  which are linear in  $\rho$ , does

not affect the values of the bulk coexistence densities. The common tangent construction can be made with or without these linear terms in  $\rho$ .

#### 4. – Nucleation, gelation, and glass transition

Whether or not the thermodynamically stable crystal phase will actually be formed depends also on kinetic effects. The crystallization may be suppressed by vitrification or gelation, and may suffer from defects, such as stacking faults and vacancies. It is therefore important to study also the kinetics, nucleation rates, and the pathways for the spontaneous formation of nuclei that can grow into the thermodynamically stable phase. Additionally, one may facilitate the formation of the ordered phases by employing external fields, like electric or magnetic fields, gravity, templates, interfaces, fluid flow, etc. This is a very active field, but outside the scope of this lecture.

#### 5. – Phase diagrams of shape-anisotropic hard particles

The methods as described in sects. **2** and **3** can be employed to determine the phase behavior of (colloidal) systems. To illustrate this, we present various phase diagrams that have been determined recently using these techniques for hard anisotropic particles. We emphasize that we focus here on phase diagrams based on free-energy calculations instead of identifying the phases that appear in direct simulations. The danger of direct simulations is that systems can get trapped in non-equilibrium structures, like gels and glasses, or in metastable ordered structures. The formation of glasses and gels, and metastable structures depends often on the history of the sample, such as the initial conditions, dynamics, etc. Consequently, a direct approach may yield conflicting results. Moreover, for phase transitions that involve large density jumps between the coexisting phases, simulation results may suffer from finite size effects due to bulk and interfacial contributions to the free energy.

**5.1. Anisotropic hard particles.** – An enormous amount of work has been devoted over the last decades on phase diagram calculations of anisotropic hard particles, such as spherocylinders, ellipsoids, cubes, cut spheres, oblate hard spherocylinders, dumbbells, polyhedral-shaped particles, etc. Exemplarily, we present phase diagrams of hard dumbbells, hard bowl-shaped particles, and hard superballs.

**5.1.1. Hard dumbbells.** The phase behaviour of hard dumbbells consisting of two fused hard spheres of diameter  $\sigma$  and their centers separated by a distance  $L$  was investigated by computer simulations in refs. [73, 74, 52, 53] as a function of the shape parameter  $L^* \equiv L/\sigma$  that defines the anisotropy of the dumbbell. Hence the model reduces to hard spheres for  $L^* = 0$  and to tangent spheres for  $L^* = 1$ . Phase diagrams of hard dumbbells as determined from computer simulations by Vega showed a stable fluid phase at low packing fraction and an orientationally ordered crystal phase (CP1 phase) at sufficiently high densities. For  $L^* < 0.4$ , a plastic crystal phase appears in the phase diagram at intermediate densities. More recently, the phase diagram was revisited by Marechal *et*

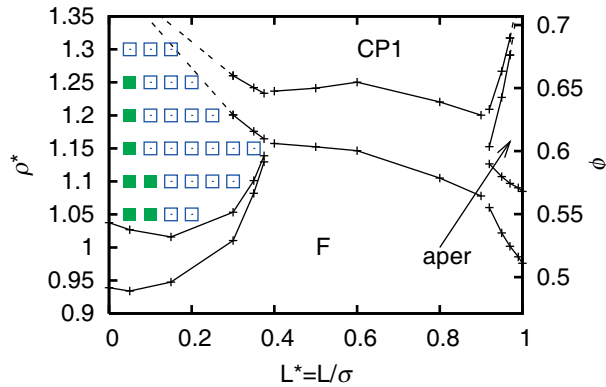


Fig. 2. – Phase diagram of hard dumbbells in reduced density  $\rho^*$  (packing fraction  $\phi$ ) versus aspect ratio  $L^* \equiv L/\sigma$  representation. F denotes the fluid phase and CP1 the periodic crystal. The aperiodic phase (aper) is stable only in a narrow region of the phase diagram. The stable FCC type plastic crystal is denoted by filled squares, the HCP plastic crystal phase is denoted by empty squares. The coexistence densities for  $L^* < 0.9$  are taken from refs. [73, 74].

*al.*, who showed that the plastic crystal with the HCP structure is more stable than the one with the FCC structure for a large part of the stable plastic crystal regime [53]. The revised phase diagram is displayed in the reduced density  $\rho^*$ - $L^*$  representation in fig. 2. Here, the dimensionless density is defined as  $\rho^* = d^3 N/V$  with  $d^3/\sigma^3 = 1 + 3L^*/2 - L^3/2$  the volume of a dumbbell divided by that of a sphere with diameter  $\sigma$ . Thus,  $d$  is the diameter of a sphere with the same volume as the dumbbell. In addition, the stability of an orientationally disordered aperiodic crystal structure in which the spheres of the dumbbells are on a random-hexagonal-close-packed lattice, and the dumbbells are formed by taking random pairs of neighboring spheres is investigated. For  $L^* > 0.88$ , the phase diagram displays a stable aperiodic crystal phase in between the stable fluid and periodic crystal phase regime [53].

**5.1.2. Hard bowl-shaped particles.** A variety of bowl-shaped colloidal particles has been synthesized in recent years [29, 75]. The phase behaviour of such a particle shape was studied by computer simulations as a function of the thickness (or equivalently deepness) of the bowl. The particles are modeled as the solid of revolution of a crescent, as this model particle captures the most important features of the colloidal bowls, a depression and a hemispherical outer shape with a diameter  $\sigma$ . The shape parameter of the bowls is defined by a reduced thickness  $D/\sigma$  of the bowl with  $D$  the thickness of the bowl, such that the model reduces to infinitely thin hemispherical surfaces for  $D/\sigma = 0$  and to solid hemispheres for  $D/\sigma = 0.5$ . Using free-energy calculations, it was shown that the phase diagram displays a stable isotropic phase, a columnar phase with polar order for sufficiently deep bowls, and four exotic crystal structures for shallow bowls, *i.e.*, IX, IB, IX', and fcc<sup>2</sup> [76, 77]. In the inverted crystal (IX) and the inverted braid-like crystal (IB), the particles are stacked in columns with half of the columns flipped upside down, such

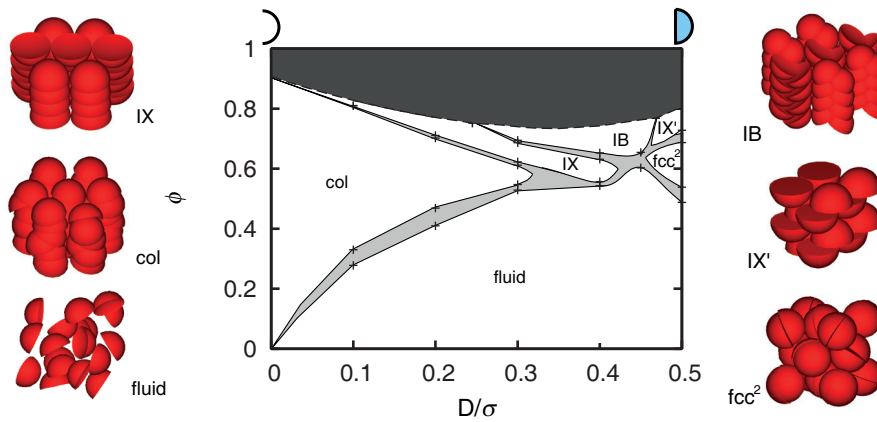


Fig. 3. – Phase diagram of hard bowl-shaped particles in the packing fraction ( $\phi$ ) versus thickness ( $D/\sigma$ ) representation. The light-gray areas denote the coexistence regions, while the dark-gray area indicates the forbidden region as it exceeds the maximum packing fraction of the bowls. The stable crystal phases, IX, IX', IB, and  $fcc^2$ , and the hexagonal columnar phase “col” are drawn schematically on the left and right of the figure. The lines are a guide to the eye.

that the rims of the bowls can interdigitate. In the IX, the columns consist of particles that are all aligned head to toe, while in the IB phase, the columns resemble braids with alternating tilt direction of the particles within each column. The solid hemispheres ( $D = 0.5\sigma$ ) display two stable crystal structures: the IX' phase can be regarded as a

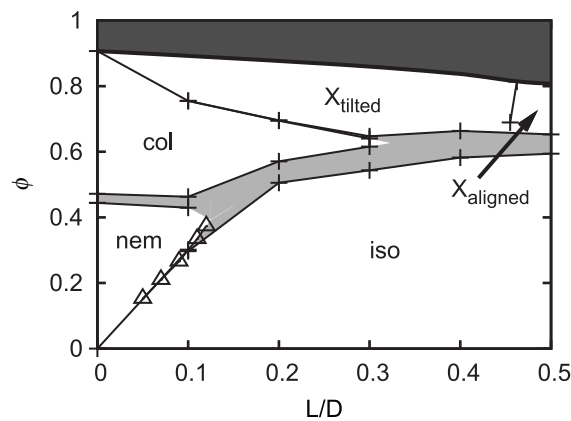


Fig. 4. – Phase diagram of oblate hard spherocylinders in the packing fraction ( $\phi$ ) versus dimensionless thickness ( $L/D$ ) representation as obtained by free-energy calculations. The state points in the dark-gray area are inaccessible since they lie above the maximum close packing line.  $X_{\text{aligned}}$  and  $X_{\text{tilted}}$ , denote the aligned and tilted crystal structures, “iso” denotes the isotropic fluid, “nem” the nematic phase, and “col” the columnar phase. The solid lines are a guide to the eye.

sheared version of IX with alternating orientation of the particles and where the particles are not organized in columns. In the paired face-centered-cubic (fcc<sup>2</sup>) phase, pairs of hemispheres join together to form complete spheres that can rotate freely on the lattice positions of an fcc crystal. The phase diagram is displayed in fig. 3 along with schematics of the different phases.

**5.1.3. Oblate hard spherocylinders.** The phase behavior of oblate hard spherocylinders, which serves as a model for colloidal hard platelets, was investigated using free-energy calculations in Monte Carlo simulations. Oblate hard spherocylinders consist of a flat cylindrical core with diameter  $\sigma$  and height  $L$ , and a toroidal rim, with tube diameter  $L$ . The total diameter of the oblate hard spherocylinder is  $D = L + \sigma$ . The phase diagram was mapped out as a function of the aspect ratio  $L/D$  of the particles [50]. The phase diagram displays a stable isotropic phase, a nematic liquid crystal phase for  $L/D \leq 0.12$ , a columnar phase for  $L/D \leq 0.3$ , a tilted crystal phase for  $L \leq 0.45$ , and an aligned crystal phase for  $L/D \geq 0.45$ , as shown in fig. 4. The phase diagram of oblate hard spherocylinders resembles that of hard cut spheres. However, the tilted crystal phase for oblate hard spherocylinders has not been found for hard cut spheres [78].

## REFERENCES

- [1] GLOTZER S. and SOLOMON M., *Nat. Mater.*, **6** (2007) 557.
- [2] SACANNA S. and PINE D. J., *Curr. Opin. Colloid. Interf. Sci.*, **16** (2011) 96.
- [3] HO C., KELLER A., ODELL J. A. and OTTEWILL R. H., *Colloid Polym. Sci.*, **271** (1993) 469.
- [4] VAN KATS C. M., JOHNSON P., VAN DEN MEERAKKER J. E. A. M. and VAN BLAADEREN A., *Langmuir*, **20** (2004) 11201.
- [5] KUIJK A., VAN BLAADEREN A. and IMHOF A., *J. Am. Chem. Soc.*, **133** (2011) 2346.
- [6] WIERENGA A., LENSTRA T. and PHILIPSE A., *Colloids Surfaces A.: Physicochem. Eng. Aspects*, **134** (1998) 8582.
- [7] PERRO A., DUGUET E., LAMBERT O., TAVEAU J.-C., BOURGEAT-LAMI E. and RAVAINÉ S., *Angew. Chem.*, **424** (2009) 361.
- [8] KRAFT D., VLUG W., VAN KATS, C.M. VAN BLAADEREN A., IMHOF A. and KEGEL W., *J. Am. Chem. Soc.*, **131** (2009) 1182.
- [9] JOHNSON P., VAN KATS C. and VAN BLAADEREN A., *Langmuir*, **21** (2005) 11510.
- [10] SUN Y. and XIA Y., *Science*, **298** (2002) 2176.
- [11] ZHANG X., DONG C., ZAPIEN J., ISMATHULLAKHAN S., KANG Z., JIE J., ZHANG X., CHANG J., LEE C.-S. and LEE S.-T., *Angew. Chem. Int. Ed.*, **48** (2009) 9121.
- [12] WU H.-L., KUO C.-H. and HUANG M. H., *Langmuir*, **26** (2010) 12307.
- [13] HENZIE J., GRÜNWARD M., WIDMER-COOPER A., GEISSLER P. and YANG P., *Nat. Mater.*, **11** (2011) 131.
- [14] EGUCHI M., MITSUI D., WU H., SATO R. and TERANISHI T., *Langmuir*, **28** (2012) 9021.
- [15] ROSSI L., SACANNA S., IRVINE W. T. M., CHAIKIN P. M., PINE D. J. and PHILIPSE A. P., *Soft Matter*, **7** (2011) 4139.
- [16] ZHANG Y., LU F., VAN DER LELIE D. and GANG O., *Phys. Rev. Lett.*, **107** (2011) 135701.
- [17] TAO A., SINSERMSUKSAKUL P. and YANG P., *Angew. Chem. Int. Ed.*, **45** (2006) 4597.
- [18] TAO A., HABAS S. and YANG P., *Small*, **4** (2008) 310.

- [19] KIM F., CONNOR S., SONG H., KUYKENDALL T. and YANG P., *Angew. Chem.*, **116** (2004) 3759.
- [20] GREYSON E. C., BARTON J. E. and ODOM T. W., *Small*, **2** (2006) 368.
- [21] DEKA S., MISZTA K., DORFS D., GENOVESE A., BERTONI G. and MANNA L., *Nano Lett.*, **10** (2010) 3770.
- [22] BRESCIA R., MISZTA K., DORFS D., MANNA L. and BERTONI G., *J. Phys. Chem. C*, **115** (2011) 20128.
- [23] MISZTA K., DE GRAAF J., BERTONI G., DORFS D., BRESCIA R., MARRAS S., CESERACCIU L., CINGOLANI R., VAN ROIJ R., DIJKSTRA M. and MANNA L., *Nat. Mater.*, **10** (2011) 872.
- [24] MANNA L., MILLIRON D., MEISEL A., SCHER E. and ALIVISATOS A., *Nat. Mater.*, **2** (2003) 382.
- [25] NEWTON M. C. and WARBURTON P. A., *Mater. Today*, **10** (2007) 1369.
- [26] ZHOU G., LÜ M., XIU Z., WANG S., ZHANG H., ZHOU Y. and WANG S., *J. Phys. Chem. B*, **110** (2006) 6543.
- [27] ZHAO N. and QI L. M., *Adv. Mater.*, **18** (2006) 359.
- [28] HUANG T., ZHAO Q. A., XIAO J. Y. and QI L. M., *ACS Nano*, **4** (2010) 4707.
- [29] ZOLDESI C. I. and IMHOF A., *Adv. Mater.*, **17** (2005) 924.
- [30] JAGADEESAN D., MANSOORI U., MANDAL P., SUNDARESAN A. and ESWARAMOORTHY M., *Angew. Chem.*, **47** (2008) 7685.
- [31] QUILLIET C., ZOLDESI C., RIERA C., VAN BLAADEREN A. and IMHOF A., *Eur. Phys. J. E*, **27** (2008) 13.
- [32] YABLONOVITCH E., *Phys. Rev. Lett.*, **58** (1987) 2059.
- [33] JOHN S., *Phys. Rev. Lett.*, **58** (1987) 2486.
- [34] VLASOV Y., BO X., STURM J. and NORRIS D., *Nature*, **414** (2001) 289.
- [35] HYNINEN A.-P., THIJSSSEN J. H. J., VERMOLEN E. C. M., DIJKSTRA M. and VAN BLAADEREN A., *Nat. Mater.*, **6** (2007) 202.
- [36] MIHI A., LÓPEZ-ALCARAZ F. and MÍGUEZ H., *Appl. Phys. Lett.*, **88** (2006) 193110.
- [37] BERMEL P., LUO C., ZENG L., KIMERLING L. and JOANNOPOULOS J., *Opt. Express*, **15** (2007) 16986.
- [38] QI H. and HEGMANN T., *J. Mater. Chem.*, **18** (2008) 3288.
- [39] FUDOUZI H. and XIA Y., *Langmuir*, **19** (2003) 9653.
- [40] YETHIRAJ A. and VAN BLAADEREN A., *Nature (London)*, **421** (2003) 513.
- [41] ZHANG Y., LU F., VAN DER LELIE D. and GANG O., *Phys. Rev. Lett.*, **107** (2011) 135701.
- [42] HAJI-AKBARI A., ENGEL M., KEYS A. S., ZHENG X., PETSCHKE R. G., PALFFY-MUHORAY P. and GLOTZER S. C., *Nature (London)*, **462** (2009) 773.
- [43] AGARWAL U. and ESCOBEDO F., *Nat. Mater.*, **10** (2011) 230.
- [44] TORQUATO S. and JIAO Y., *Nature (London)*, **460** (2009) 876.
- [45] HALES T. C. and FERGUSON S. P., *Discrete Comput. Geom.*, **36** (2006) 5.
- [46] DE GRAAF J., VAN ROIJ R. and DIJKSTRA M., *Phys. Rev. Lett.*, **107** (2011) 155501.
- [47] JIAO Y., STILLINGER F. H. and TORQUATO S., *Phys. Rev. E*, **79** (2009) 041309.
- [48] JIAO Y., STILLINGER F. H. and TORQUATO S., *Phys. Rev. E*, **84** (2011) 069902.
- [49] BATTEN R. D., STILLINGER F. H. and TORQUATO S., *Phys. Rev. E*, **81** (2010) 061105.
- [50] MARECHAL M., CUETOS A., MARTINEZ-HAYA B. and DIJKSTRA M., *J. Chem. Phys.*, **134** (2011) 094501.
- [51] SMALLENBURG F., FILION L., MARECHAL M. and DIJKSTRA M., *Proc. Natl. Acad. Sci. U.S.A.*, **109** (2012) 17886.
- [52] VEGA C. and MONSON P. A., *J. Chem. Phys.*, **107** (1997) 2696.
- [53] MARECHAL M. and DIJKSTRA M., *Phys. Rev. E*, **77** (2008) 061405.
- [54] BOLHUIS P. and FRENKEL D., *J. Chem. Phys.*, **106** (1997) 666.

- [55] WOODLEY S. M. and CATLOW R., *Nat. Mater.*, **7** (2008) 937.
- [56] MADDOX J., *Nature*, **335** (1988) 201.
- [57] PANNETIER J., BASSAS-ALSINA J., RODRIGUEZ-CARVAJAL J. and CAIGNAERT V., *Nature*, **346** (1990) 343.
- [58] KARFUNKEL H. R. and GDANITZ R. J., *J. Comput. Chem.*, **13** (1992) 1171.
- [59] OGANOV A. R. and GLASS C. W., *J. Chem. Phys.*, **124** (2006) 244704.
- [60] STUCKE D. P. and CRESPI V. H., *Nano Lett.*, **3** (2003) 1183.
- [61] D. G., KAHL G. and LIKOS C., *J. Chem. Phys.*, **122** (2005) 204503.
- [62] WALES D. and SCHERAGA H., *Science*, **285** (1999) 1368.
- [63] FILION L., MARECHAL M., VAN OORSCHOT B., PELT D., SMALLENBURG F. and DIJKSTRA M., *Phys. Rev. Lett.*, **103** (2009) 188302.
- [64] BIANCHI E., DOPPELBAUER G., FILION L., DIJKSTRA M. and KAHL G., *J. Chem. Phys.*, **136** (2012) 214102.
- [65] DE GRAAF J., VAN ROIJ R. and DIJKSTRA M., *Phys. Rev. Lett.*, **107** (2011) 155501.
- [66] MARTOŇÁK, R. LAIO A. and PARRINELLO M., *Phys. Rev. Lett.*, **90** (2003) 075503.
- [67] FRENKEL D. and SMIT B., *Understanding Molecular Simulation: From Algorithms to Applications*, 2nd edition (Academic Press, London) 2002.
- [68] FRENKEL D. and LADD A., *J. Chem. Phys.*, **81** (1984) 3188.
- [69] FORTINI A., DIJKSTRA M., SCHMIDT M. and WESSELS P. P. F., *Phys. Rev. E*, **71** (2005) 051403.
- [70] NI R., GANTAPARA A., DE GRAAF J., VAN ROIJ R. and DIJKSTRA M., *Soft Matter*, **8** (2012) 12135.
- [71] ALLEN M., EVANS G., FRENKEL D. and MULDER B., *Adv. Chem. Phys.*, **86** (1993) 1.
- [72] NOYA E., VEGA C., DOYE J. and LOUIS A., *J. Chem. Phys.*, **127** (2007) 054501.
- [73] VEGA C., PARAS E. P. A. and MONSON P. A., *J. Chem. Phys.*, **96** (1992) 9060.
- [74] VEGA C., PARAS E. P. A. and MONSON P. A., *J. Chem. Phys.*, **97** (1992) 8543.
- [75] XIA Y., GATES B. and LI Z., *Adv. Mater.*, **13** (2001) 109.
- [76] MARECHAL M., KORTSCHOT R. J., DEMIRÖRS A. F., IMHOF A. and DIJKSTRA M., *Nano Lett.*, **10** (2010) 1907.
- [77] MARECHAL M. and DIJKSTRA M., *Phys. Rev. E*, **82** (2010) 031405.
- [78] VEERMAN J. A. C. and FRENKEL D., *Phys. Rev. A*, **45** (1992) 5632.